

Available at www.sciencedirect.com

ScienceDirect

journal homepage: www.elsevier.com/locate/carbon

Hierarchically porous carbon by activation of shiitake mushroom for capacitive energy storage

Ping Cheng, Shuangyan Gao, Peiyu Zang, Xiaofan Yang, Yonglong Bai, Hua Xu, Zonghuai Liu, Zhibin Lei *

School of Materials Science and Engineering, Shaanxi Normal University, 620 West Chang'an Street, Xi'an, Shaanxi 710119, China

ARTICLE INFO

Article history:

Received 29 January 2015

Accepted 13 May 2015

Available online 22 May 2015

ABSTRACT

We present a facile yet effective two-step activation method to prepare a hierarchically porous carbon with natural shiitake mushroom as the starting materials. The first step involves the activation of shiitake mushroom with H_3PO_4 , while the second step is to further activate the product with KOH. The resulting carbon is comprised of abundant micro-, mesopores and interconnected macropores that has a specific surface area up to $2988 \text{ m}^2 \text{ g}^{-1}$ and pore volume of $1.76 \text{ cm}^3 \text{ g}^{-1}$. With the unique porous nature, the carbon exhibited a specific capacitance of 306 and 149 F g^{-1} in aqueous and organic electrolyte, respectively. Moreover, this carbon also shows a high capacitance retention of 77% at large current density of 30 A g^{-1} and exhibited an outstanding cycling stability with 95.7% capacitance preservation after 15,000 cycles in 6 M KOH electrolyte. The far superior performance as compared with those of the commercially most used activated carbon RP20 in both aqueous and non-aqueous electrolyte demonstrates its great potential as high-performance supercapacitor electrode. The two-step method developed herein also represents a very attractive approach for scalable production of various functional carbon materials using diverse biomasses as starting materials.

© 2015 Elsevier Ltd. All rights reserved.

1. Introduction

Supercapacitors have been received increasing attentions during the past decades in view of their unique features including ultrahigh power density, fast charge–discharge rate, and exceptionally long cycling stability [1,2]. Supercapacitor stores energy by electrical double-layer capacitance (EDLC) formed on the electrode surface or through reversible Faradic redox reaction occurring at the electrolyte/electrode interface. The fast charge–discharge character enables supercapacitors to be one of the most promising power supplies that hold great promises in various hybrid electric vehicles,

portable equipments and electronic devices [3,4]. It is well known that the performance of a supercapacitor strongly depends on the nature of the active materials. Carbon materials with different dimensions, like carbon onions, one-dimensional CNTs, two-dimensional graphene and three-dimensional (3D) carbon-derived carbides, have been extensively explored as supercapacitor electrode because of their good electronic conductivities, facilely controlled pore structures and tailorable surface chemistries [4–9]. Among these carbon materials, activated carbons (ACs) show competitive advantages in supercapacitor industry as they have low

* Corresponding author at: School of Materials Science and Engineering, Shaanxi Normal University, 199 South Chang'an Road, Xi'an, Shaanxi 710062, China. Fax: +86 29 81530702.

E-mail address: zblei@snnu.edu.cn (Z. Lei).

<http://dx.doi.org/10.1016/j.carbon.2015.05.056>

0008-6223/© 2015 Elsevier Ltd. All rights reserved.

production costs, very large specific surface areas (SSA) and exceptional electrochemical cycling stabilities [10,11].

Carbonization of natural products represents a facile and cost-effective route toward scalable production of ACs for application in waste water treatment [12], biosensor [13] and energy storage and conversion [14–20]. Up to now, carbon materials with various macroscopic morphologies and tailorable structures have been developed by using various natural biomass as starting materials [21]. For instance, thermal carbonization of watermelon could yield mechanically flexible and chemically active carbon aerogel, which has been demonstrated to be an excellent scaffold to incorporate Fe_3O_4 nanoparticles for pseudocapacitor [22]. Hydrothermal treatment of the used bamboo chopsticks in alkaline solution, followed by a high-temperature carbonization generated carbon fibers which showed enhanced performance in Li-ion batteries after coating of nanostructured MnO_2 [23]. Most recently, crab shell consisting of highly mineralized chitin-protein fibers was also utilized as biotemplate to prepare hollow carbon nanofibers arrays for potential application in Li-ion battery and supercapacitors [24,25]. In addition, plant biomass including *Typha orientalis* [14], banana peels [26], celutec leaves [27] and ginkgo shells [28] have also been utilized as starting materials to prepare various carbon products.

For carbon materials used in supercapacitors, their pore sizes and distributions play important roles in capacitive performances [29]. ACs used in the current supercapacitor industry are primarily composed of micropores with majority of pore size below 2.0 nm. Such structure limitation results in a long ion pathway and a large diffusion resistance, leading to a low charge storage capability and poor capacitance retention especially at very high discharge rate. To enable the AC-based supercapacitor to meet the requirement of high-performance energy storage devices, AC electrode comprising of micro-, meso- and macropores is highly desirable [30–32] as the macropores usually serve as ion buffer reservoirs for shortening the ion diffusion length, whereas the abundant micro- and mesopores are essential for improving the charge storage capability, leading to a simultaneous achievement of both high energy density and high power density [33].

Herein, we presented a facile yet effective two-step approach to prepare a highly porous AC for capacitive energy storage utilizing natural shiitake mushroom as the starting materials. As illustrated in Fig. 1, in the first step H_3PO_4 was used as an activation agent to preliminarily activate shiitake mushroom at 500 °C because of its mild oxidation ability [34,35]. This step yielded a carbon product composed of aggregated carbon nanoparticles with disordered texture porosity. The second step involved a further activation of H_3PO_4 -

activated product with KOH at 800 °C. The resultant carbon undergoing such two-step process displayed a high SSA of $2988 \text{ m}^2 \text{ g}^{-1}$, composing of small micro- and mesopores in the range of 1.5–8.0 nm and large macropores varying from tens of nanometers to a few hundred nanometers. The carbon material exhibited a specific capacitance of 306 F g^{-1} at 1.0 A g^{-1} in 6 M KOH aqueous electrolyte, with a remarkable capacitance retention of 78.4% at a high current density of 30 A g^{-1} . Moreover, it also showed a specific capacitance of 149 F g^{-1} with a good rate performance in tetraethylammonium tetrafluoroborate (TEABF_4) in acetonitrile (AN) (TEABF_4/AN). These results are much superior to those of the commercially most used AC product RP20, making the present two-step method a promising technique for preparing highly active carbon with great potentials in electrochemical energy storage with various natural biomasses as starting materials.

2. Experimental

2.1. Samples preparation

The commercially available shiitake mushroom was washed by immersing into hot water for 2 h under stirring, followed by splitting into small pieces with dimensions of $3 \text{ mm} \times 3 \text{ mm} \times 2 \text{ mm}$, and drying at 60 °C for 24 h. Afterward, 1.0 g of the dried shiitake mushroom was soaked into 5.0 mL water containing 3 mL of concentrated H_3PO_4 (85 wt%). After evaporation of water by heating the mixture at 150 °C in an oil bath, the viscous and dark-brown product was collected and transferred into a ceramic boat. The activation treatment was conducting at 500 °C for 2 h in flowing N_2 . Removal of the excessive acid with copious water and ethanol, followed by filtration and drying yielded the black product which was denoted as PAC-500. In control experiment, the obtained PAC-500 was thermally annealed at 800 °C for 2 h in flowing N_2 to get a sample named as PAC-800. For comparison, we also directly pyrolyzed the dried shiitake mushroom at 800 °C without use of any activation agents. This sample was denoted as AC-800.

The PAC-500 sample collected in the first step was subject to an activation process in the second step with KOH as activation agents. Typically, PAC-500 of 0.3 g was added into 2.0 M KOH aqueous solution to achieve a mass ratio of $\text{KOH}/\text{PAC-500} = 3$. After evaporation of the excessive water at 120 °C, the PAC-500/KOH mixture was heated in N_2 at 800 °C for 2 h with a ramp rate of $5 \text{ }^\circ\text{C min}^{-1}$. The product was washed with 2.0 M HCl and copious water until the pH of the filtrate reached 7. The collected sample was denoted as KPAC-800.



Fig. 1 – Schematic illustration of the two-step procedure for preparing a highly porous carbon with shiitake mushroom as starting materials. (A color version of this figure can be viewed online.)

2.2. Characterization methods

The morphologies of the samples were examined by field-emission scanning electron microscopy (FESEM) on SU8020. The microstructures of the samples were observed on Tecnai G2 F20 S-Twin Field-emission transmission electron microscopy (FETEM) operated at an acceleration voltage of 200 kV. Nitrogen adsorption/desorption isotherms were measured at 77 K on a micromeritics ASAP 2420 analyzer. Samples were degassed at 180 °C for 8 h prior to the measurement. The SSA of the samples was determined using the Brunauer–Emmett–Teller (BET) method with the adsorption data at the relative pressure (P/P_0) range of 0.05–0.2. The total pore volumes were estimated at $P/P_0 = 0.99$. The pore size distribution (PSD) was analyzed using a nonlocal density functional theory (NLDFT) model assuming the cylinder pore geometry from the adsorption data. X-ray photoelectron spectroscopy (XPS) spectra were collected on an AXIS ULTRA spectrometer (Kratos Analytical) using a monochromatized Al K α X-ray source (1486.71 eV). Raman spectra were measured on a Renishaw inVia Raman microscope with an excitation wavelength of 532 nm.

2.3. Electrochemical measurements

The electrochemical performances of the electrode materials were characterized by cyclic voltammetry (CV), galvanostatic charge–discharge and electrochemical impedance spectroscopy (EIS) on a Gamary Reference 3000 electrochemical workstation. Both 6.0 M KOH aqueous solution and 1.0 M TEABF $_4$ /AN were used as electrolyte. The working electrode was prepared by mixing an active material (90 wt%) with carbon black (5 wt%) and polytetrafluoroethylene (PTFE, 5 wt%) in water. The slurry of the mixture was painted between two pieces of nickel foam (1.2 cm 2) and then pressed under a pressure of 100 kg cm $^{-2}$. The mass loading for each electrode is typically of 2.0 mg cm $^{-2}$. In a three-electrode system, a Pt foil and a Ag/AgCl electrode were applied as the counter

and reference electrodes, respectively. The specific capacitance, C (F g $^{-1}$) of the electrode material was calculated from the galvanostatic discharge curves according to the following equation: $C = I \times \Delta t / (\Delta V \times m)$, where I is the discharge current (A), Δt is the discharge time (s), ΔV is the voltage change (V) excluding voltage drop (IR drop) in the discharge process, and m is the mass of the active material (g). In a two-electrode cell, a Swagelock-type capacitor was configured with Celgard[®]3501 as the separator. The specific capacitance was calculated according to the equation: $C_s = 4 \times I \times \Delta t / (\Delta V \times m)$, where I , Δt and ΔV are discharge current (A), discharge time (s) and the voltage change (V) excluding the IR drop during the discharge process, respectively. Whereas, m is the total mass of the active material (g) in two electrodes. The energy density and power density of a supercapacitor was determined by using $E = 0.5CV^2/3.6$ and $P = 3600E/t$, where E is the energy density (Wh kg $^{-1}$), P is the power density (kW kg $^{-1}$), C is the specific capacitance measured using a two-electrode cell (F g $^{-1}$), V is the actual voltage excluding IR drop (V), and t is the discharging time (s) [36]. The ion kinetics within an electrode material is investigated by electrochemical impedance spectroscopy (EIS) with an amplitude of 10 mV at the frequency range of 0.005 Hz to 100 kHz.

3. Results and discussion

Shiitake mushroom is a member of edible fungi that composed of vitamin, protein, and nitrogen-containing compounds. SEM images shows that it is comprised of uniform carbonaceous belts with typical 200 μ m in length and 20 μ m in width (Fig. S1). The opened porous texture formed by aggregated carbonaceous belts allows full penetration of H $_3$ PO $_4$ molecules into its interior structure and makes the first activation step more sufficiently. Fig. S2 shows the morphologies of the resultant carbon samples obtained in the first step. Both PAC-500 and PAC-800 display irregular monolithic morphology with an individual size varying from several to tens of micrometers. A close examination reveals that each carbon

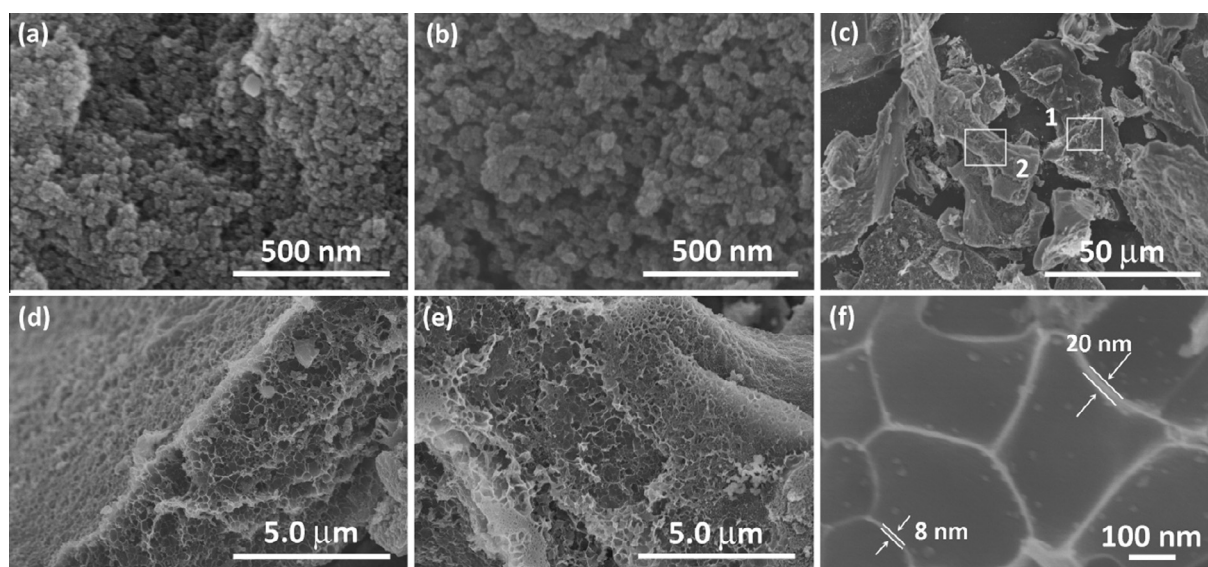


Fig. 2 – FESEM image of PAC-500 (a), PAC-800 (b) and KPAC-800 (c–f) with low (c–e) and high (f) magnifications.

monolith is actually composed of numerous carbon particles with particle size of 20–50 nm (Fig. 2a and b). These carbon nanoparticles are aggregated together to form numerous textural porosities which facilitate the access of KOH into the interior structure of PAC-500 for subsequent activation. The KPAC-800 after KOH activation displays similar macroscopic morphology to PAC-500 (Figs. 2c and S2). Region 1 and region 2 in Fig. 2c were magnified in Fig. 2d and e, respectively. Markedly differing from the aggregated carbon nanoparticles produced in the first step, the KPAC-800 displays a hierarchically porous network composed of interconnected macropores on both cross-sectional (Fig. 2d) and surface area (Fig. 2e). The macropores pore size ranges from tens of nanometers to a few hundred nanometers with pore wall thickness of 8–20 nm (Fig. 2f). This observation shows that activation of PAC-500 with KOH potentially induce the structure transformation. A presumable reason for this observation is that the abundant textural porosities of PAC-500 provide numerous channels for permeation of KOH in the bulk and on its surface. The synergistic etching of carbon atoms inward and outward induce the conversion of particle-like PAC-500 into hierarchical porous KPAC-800 [37]. Fig. 3 shows the HRTEM images of KPAC-800 with different magnifications. Hierarchically porous framework including macropores and numerous mesopores can be clearly seen from the low-magnification images (Fig. 3a and b), in good

consistence with the SEM images (Fig. 2d and e). A close examination reveals that KPAC-800 is composed of disordered and wormlike porosity throughout the whole structure. Both micropores and mesopores were homogeneously distributed in the carbon matrix (Fig. 3c). The curved graphene layers with a large interlayer spacing of 0.398 nm (Fig. 3d) suggest a low graphitization of KPAC-800, which is likely due to a harsh oxidation of carbon atoms with KOH at 800 °C.

The porous structure of the carbon product was characterized by N₂ adsorption/desorption. Sample PAC-500 exhibits a continuous N₂ uptake with the increase of the relative pressure (Fig. 4a). The distinct hysteresis loop occurred at high relative pressure of $P/P_0 > 0.7$ indicates the existence of textural porosities, agreeing well with the aggregated carbon particles as indicated in Fig. 2a. The PAC-500 gives no characteristic PSD peaks with a pore size range from 2.0 to 5.0 nm (Fig. 4b). Considering the reaction between H₃PO₄ and carbon atoms is thermodynamically favorable at a temperature above 750 °C [35], the formation of these nanopores at 500 °C in the first step is probably achieved through dehydration of the cellulose, hemicelluloses and lignin with H₃PO₄ [35,38]. On the basis of the N₂ adsorption, the SSA and pore volume of PAC-500 were determined to be 1341 m² g⁻¹ and 2.02 cm³ g⁻¹, respectively (Table 1). In contrast, a very low N₂ uptake of AC-800 suggests nonporous nature because of the direct pyrolysis of shiitake mushroom

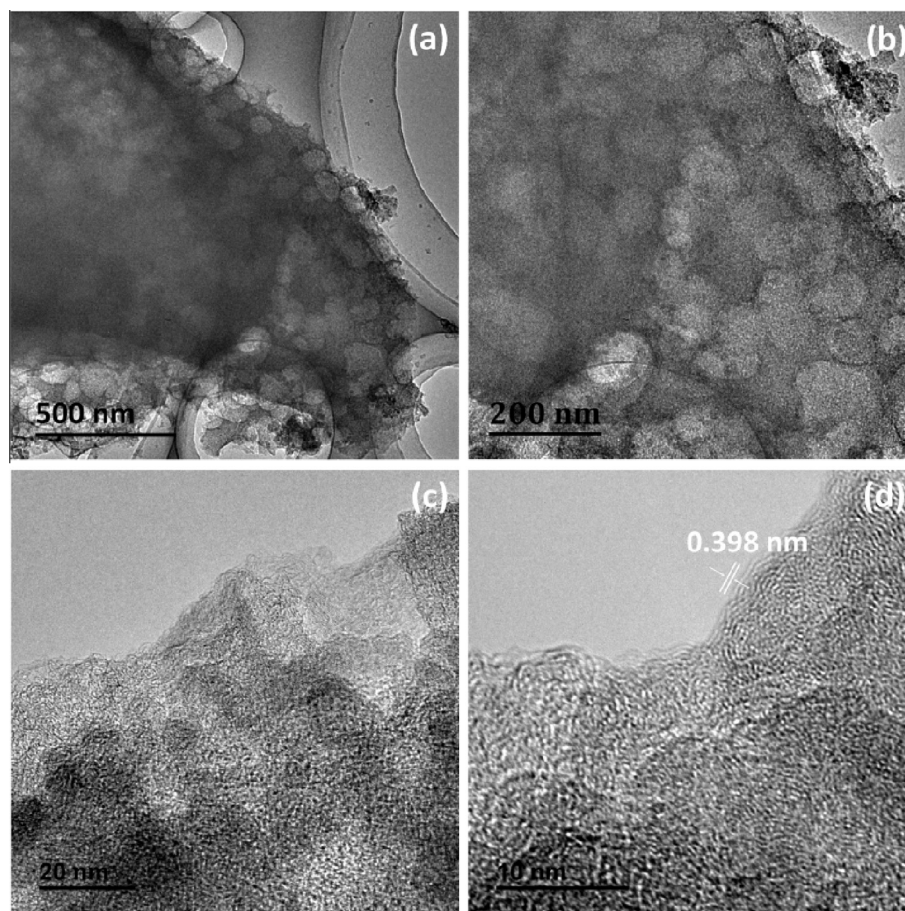


Fig. 3 – TEM image of KPAC-800 with low (a and b) and high (c and d) magnifications.

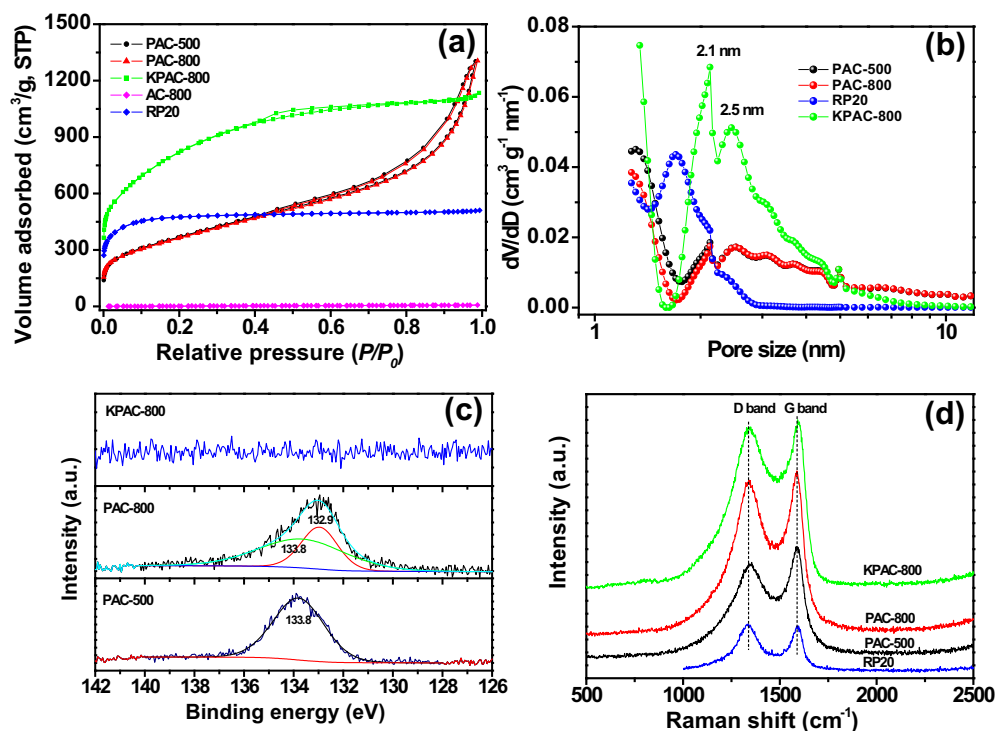


Fig. 4 – N₂ adsorption/desorption isotherm (a), PSD determined from NLDFT (b), deconvoluted P 2p XPS spectra (c) and Raman spectra (d) of carbon samples prepared at different conditions. (A color version of this figure can be viewed online.)

without use of any activation agents. This comparison highlights the role of H₃PO₄ in developing the nanopores. By comparing the SEM images of PAC-500 and PAC-800 (Fig. 2a and b), and their corresponding N₂ adsorption and PSD (Fig. 4a and b), it is concluded that thermal annealing of PAC-500 at 800 °C does not destroy both the macroscopic morphology and microstructure (Fig. S2), suggesting a good thermal stability of the obtained carbon framework.

The KPAC-800 after KOH activation in the second step displays a moderate N₂ adsorption below $P/P_0 < 0.1$ and a differentiable hysteresis loop at relative pressure region of $0.4 < P/P_0 < 0.6$, indicating formation of both micropores and mesopores. However, the textural porosities formed in the first step disappear after KOH activation. These variations agree well with the morphology change as shown in Fig. 2. Given that the activation process is achieved through a chemical reaction between KOH and carbon atoms: $6\text{KOH} + \text{C} \rightarrow 2\text{K} + 3\text{H}_2 + 2\text{K}_2\text{CO}_3$ [28,39,40], etching of carbon atoms with KOH is usually accompanied with partial structure collapse. Such process leads to a decreased pore volume to 1.76 cm³ g⁻¹ (Table 1). The PSD of KPAC-800 displays well-developed peaks centered at 2.1 and 2.5 nm, and a prominent mesopores range from 2.5 to 8.0 nm (Fig. 4b). Due to the large contribution of micropores to the SSA, a twofold enhanced SSA (2988 m² g⁻¹) was measured for KPAC-800 (Table 1). In a control experiment, activation of nonporous AC-800 with KOH only yielded porous carbon with a moderate SSA (1081 m² g⁻¹) and pore volume (0.55 cm³ g⁻¹) (Fig. S3). This result clearly demonstrates that formation of nanopores by H₃PO₄ activation in the first step is of great importance for the subsequent KOH activation as nanopores created by

H₃PO₄ activation could provide abundant channels to accommodate KOH, making the dispersion of activation agents within the porosities of PAC-500 more homogeneously and the following activation step more effectively. Unlike most of KOH-activated carbons that are predominated by micropores [19,28,41], the KPAC-800 prepared by the two-step route contains only 40% micropores (0.71 cm³ g⁻¹) according to the NLDFT structure analysis (Table 1). It is noted that the hierarchically porous framework that combines the macro-, meso- and micropores is of great importance for a high-performance supercapacitor as the macropores and mesopores dramatically improve the ion kinetics, while the abundant micropores are essential for boosting the charge storage capacity.

The element compositions of the products were examined by XPS. Three elements of C, O and P were detected in PAC-500 and PAC-800, while only C and O signals were found in KPAC-800 sample (Fig. S4). The deconvoluted P 2p XPS spectra with a binding energy of 133.8 eV relevant to the phosphate is found to slightly shifts toward a lower binding energy (132.9 eV) upon increasing the carbonization temperature (Fig. 4c), suggesting conversion of phosphate into polyphosphate due to gradual dehydration and condensation of H₃PO₄ [42]. A similar result was also described in a H₃PO₄-activated carbon with sisal and polymers as carbonaceous precursors [42,43]. As summarized in Table 1, thermal annealing of PAC-500 at 800 °C reduces both O and P contents, whereas, KOH activation step increases the O content but eliminate the element P. This change was further verified by Raman spectra in Fig. 4d. For all three samples, two characteristic bands at 1340 cm⁻¹ (D band) and 1590 cm⁻¹ (G band)

Table 1 – Structure parameters of carbon samples and their capacitive performances.

Samples	Element composition (at.%)			S_{BET} ($\text{m}^2 \text{g}^{-1}$)	V_t^a ($\text{cm}^3 \text{g}^{-1}$)	V_{mic}^b ($\text{cm}^3 \text{g}^{-1}$)	I_D/I_G	Specific capacitance ^c (F g^{-1})	Capacitance retention (%) (30 A g^{-1})
	C	O	P						
PAC-500	90.1	7.2	2.7	1341	2.02	0.28	0.83	196	59.3
PAC-800	92.2	6.0	1.8	1315	2.02	0.28	0.94	196	75.8
KPAC-800	91.1	8.9	–	2988	1.76	0.71	0.97	306	78.4
RP20	89.0	11.0	–	1628	0.79	0.67	1.02	163	75.8

^a Total pore volume measured at relative pressure of 0.99.^b Micropore volume (pore size <2 nm) analyzed from NLDFT.^c Specific capacitance measured at current density of 1.0 A g^{-1} in three-electrode cell with 6.0 M KOH as an aqueous electrolyte.

can be clearly seen. The former corresponds to the sp^3 carbon atoms of disordered or defective carbon, while the latter is a characteristic feature of sp^2 -hybridized carbon atoms from graphitic layers. By comparing the Raman spectra of PAC-800 and KPAC-800, a slight increase of intensity ratio (I_D/I_G) from 0.94 to 0.97 (Table 1) reveals more defects were introduced in KPAC-800 due to the oxidation of carbon atoms with KOH, leaving behind rich oxygen-containing functional groups as indicated by a high oxygen content of KPAC-800 from XPS quantitative analysis (Table 1).

The electrocapacitive performances of the obtained carbon materials were investigated in a three-electrode system with 6.0 M KOH as an aqueous electrolyte. Fig. 5a shows the CV curves of PAC-500, PAC-800 and KPAC-800 electrode at a scan rate of 50 mV s^{-1} . Both PAC-500 and PAC-800 electrodes show similar CV profiles except that PAC-800 exhibits a slightly improved rectangular shape as indicated by the steep current change (Fig. 5a). As PAC-800 has a similar pore structure to PAC-500, this improvement suggests less contribution of pseudocapacitance because of the deoxygenation during thermal annealing process. By contrast, the KPAC-800 electrode exhibits a markedly enhanced current response with a perfect rectangular profile, indicating an increased specific capacitance and a good rate performance. The galvanostatic charge–discharge curves of the three samples at 1.0 A g^{-1} were compared in Fig. 5b and their specific capacitance were listed in Table 1. Both PAC-500 and PAC-800 electrode exhibit the same capacitance value of 196 F g^{-1} . However, a significantly enhanced capacitance of 306 F g^{-1} was achieved for KPAC-800 electrode, which is much higher than those of the counterparts by carbonizing other biomasses [28,44,45]. Moreover, upon increasing the current density to 30 A g^{-1} , specific capacitance of 240, 148 and 116 F g^{-1} were still retained for KPAC-800, PAC-800 and PAC-500 electrode (Fig. 5c), corresponding to capacitance retention of 78.4%, 75.8% and 59.3%, respectively (Table 1). The performance of RP20 [31,46], one of most used AC in supercapacitor industry, was also tested under the identical condition and its performance was included in Table 1. The far superior performance of KPAC-800 as compared with RP20 demonstrates its great potential as a promising electrode material for supercapacitor application.

In order to demonstrate the superior performance of KPAC-800 electrode for electrochemical energy storage, we fabricated a symmetric KPAC-800 capacitor and tested its capacitive performance using a best practice method recommended by Ruoff et al. [47]. Fig. 6a compares the CV curves of KPAC-800 and RP20 at a scan rate of 50 mV s^{-1} in 6.0 M KOH. The dramatically enhanced current response and the rectangular CV shape suggest more energy can be stored in KPAC-800 electrode through a fast ion adsorption mechanism. Moreover, the KPAC-800 electrode exhibits an outstanding rate capability as indicated by the perfect rectangular CV shape even at a very high scan rate of 400 mV s^{-1} (Fig. 6b). Fig. 6c shows the charge–discharge curves of KPAC-800-based capacitor at different current densities. The symmetric charge and discharge curves demonstrate its ideal capacitive behavior due to ion adsorption at the carbon electrode surface. The specific capacitances of KPAC-800 electrode calculated from the discharge curves were compared with those

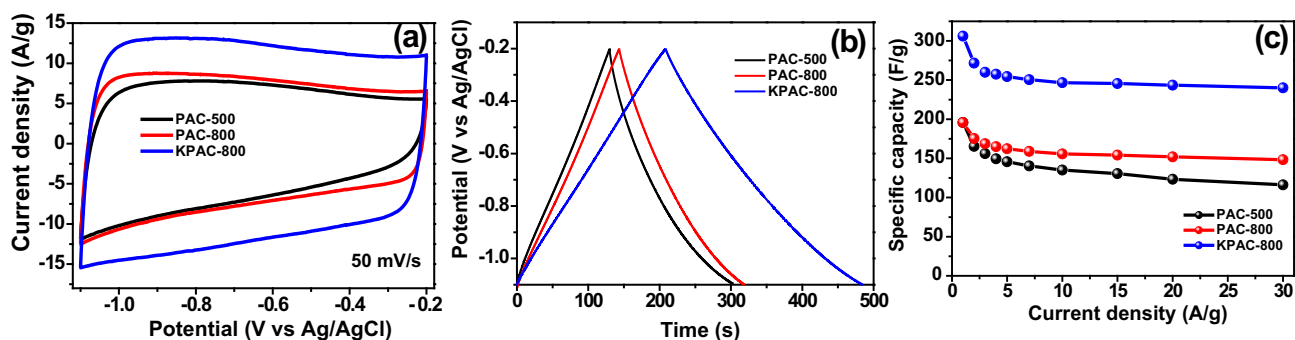


Fig. 5 – Electrochemical performances of activated carbon electrodes in three-electrode cell with 6.0 M KOH as aqueous electrolyte. (a) CV, (b) galvanostatic charge–discharge at 1.0 A g^{-1} , and (c) capacitance retention at different current densities. (A color version of this figure can be viewed online.)

of RP20 in Fig. 6d. KPAC-800 electrode delivers a specific capacitance of 238 F g^{-1} at a current density of 0.2 A g^{-1} , and retains a high capacitance of 178 F g^{-1} at a current density of 30 A g^{-1} . Whereas, RP20 electrode delivers a much lower capacitance of 132 F g^{-1} at 0.2 A g^{-1} , and rapidly decrease to 60.4 F g^{-1} at 30 A g^{-1} . The high specific capacitance and 75% capacitance retention clearly demonstrate that the hierarchical KPAC-800 comprising of micro-, meso- and macropores potentially favors ion kinetics, leading to a high utilization efficiency of electrode materials for EDLC formation.

The easy access of electrolyte ions within KPAC-800 electrode was also verified by the EIS. Fig. 6e shows the dependence of impedance phase angle on the frequency of KPAC-800 and RP20 electrode. The relaxation time constant τ_0 of

capacitor, as defined by $\tau_0 = 1/f_0$ at a phase angle of -45° , represents the transition between a capacitive behavior and a resistive behavior [48]. Consequently, τ_0 can be used as a quantitative measure to evaluate how fast a supercapacitor device can be discharged. The RP20 electrode has a τ_0 of 2.45 s, a typical value for microporous or mesoporous AC-based supercapacitor [48,49]. However, KPAC-800 electrode exhibits a very short time constant of 0.71 s. This value is nearly equal to 0.73 s of graphene aerogel electrode [34], and comparable to 0.47 s of graphene nanomesh electrode [50], and 0.49 s of graphene framework electrode [51]. The very short τ_0 as compared with that of conventional AC highlights the favorable structure of hierarchical KPAC-800 for ion motions. The interconnected macropores serve as ion buffer reservoir, while the very thin wall thickness (8–20 nm) greatly

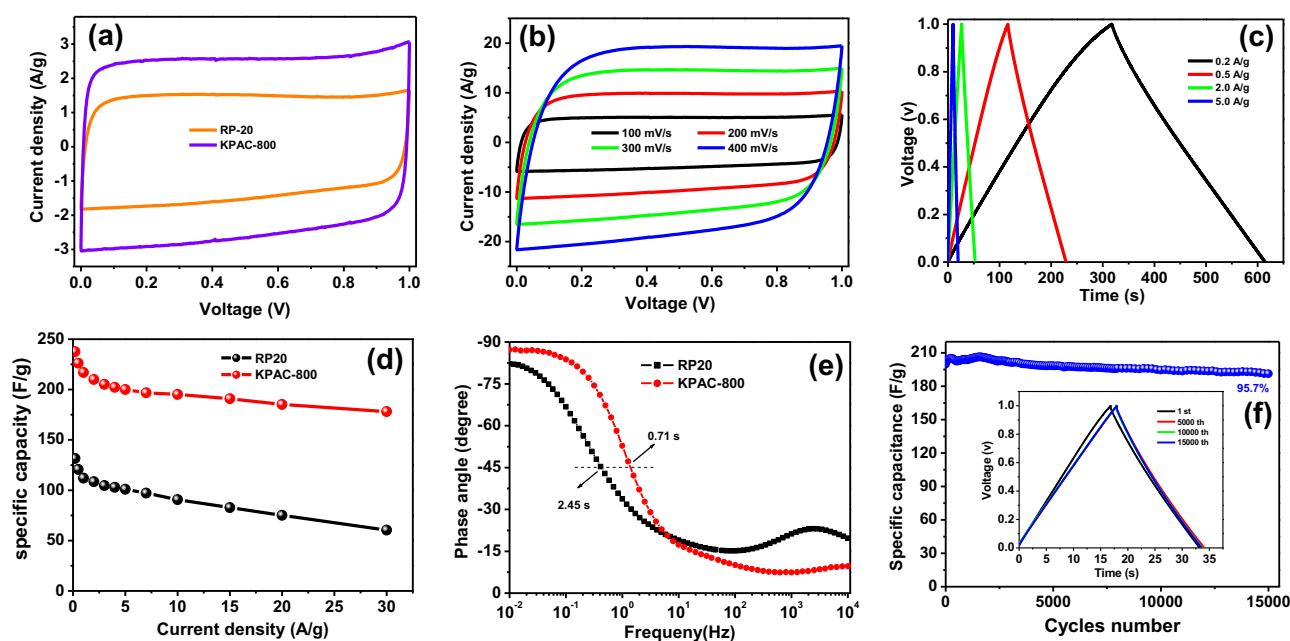


Fig. 6 – Capacitive performance of symmetric KPAC-800 and RP20 electrode in 6.0 M KOH aqueous electrolyte. (a) CV curves at scan rate of 50 mV s^{-1} . (b) CV and (c) charge–discharge profiles of KPAC-800. (d) Capacitance retention and (e) Bode plots of phase angle versus frequency of KPAC-800 and RP20 electrode. (f) Cycling stability of KPAC-800 electrode at current density of 3.0 A g^{-1} . The inset in (f) shows the charge–discharge curves of different cycles. (A color version of this figure can be viewed online.)

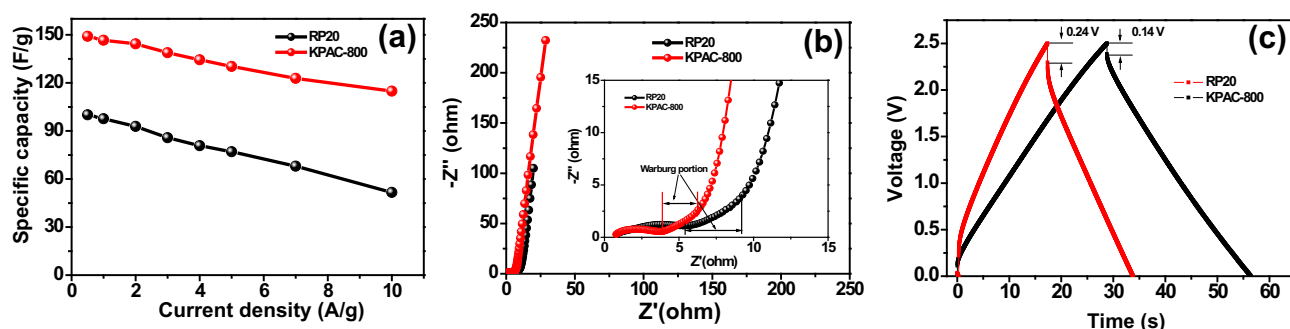


Fig. 7 – Capacitive performance of symmetric KPAC-800 and RP20 electrode in 1.0 M TEABF₄/AN electrolyte. (a) Capacitance retention at various current densities. (b) Nyquist plots of KPAC-800 and RP20 electrodes with inset showing the high-frequency region. (c) Charge–discharge curves of KPAC-800 and RP20 electrode at current density of 3.0 A g⁻¹. (A color version of this figure can be viewed online.)

shortens the ion pathway, thus enabling most of the micropores to be easily accessed by electrolyte ion for charge storage. Besides a high specific capacitance and an outstanding rate capability, the KPAC-800 electrode also exhibits an extraordinary cycling performance with 95.7% capacitance retention after 15,000 cycles of consecutive charge–discharge at 3.0 A g⁻¹ (Fig. 6f). The nearly identical charge discharge curves (inset in Fig. 6f) confirm its electrochemical stability, which is an intrinsic character of a double-layer capacitor.

The capacitive performances of KPAC-800 were also compared with RP20 in 1.0 M TEABF₄/AN organic electrolyte. Specific capacitance of 149 and 115 F g⁻¹ were achieved for KPAC-800 at 0.5 and 10 A g⁻¹, respectively (Fig. 7a). The relatively lower specific capacitance measured in organic electrolyte indicates that the micropores with smaller size are not fully accessed by the large solvated ion of TEABF₄/AN (1.3 nm for TEA⁺ and 1.16 nm for BF₄⁻ in acetonitrile vs. 0.334 nm of K⁺ in water) [50,52,53], thus hindering formation of double layer at the electrolyte/electrode interface. Nevertheless, the capacitance value is still higher than 120 F g⁻¹ of activated reduced graphene oxides film electrode [54], 140 F g⁻¹ of graphene nanomesh electrode [50], and even comparable to 154 F g⁻¹ of KOH activated microwave exfoliated graphene oxide (a-MEGO) [39]. In contrast, the RP20 electrode under the identical condition displayed a capacitance of

100 and 52 F g⁻¹. Fig. 7b compares the Nyquist plots of the KPAC-800 and RP20 electrode in TEABF₄/AN. In spite of both electrodes displaying capacitive behaviors at low frequency region, the obviously smaller Warburg portion of KPAC-800 at middle frequency range (inset in Fig. 7b) reveals smaller ion diffusion resistance within the hierarchically porous network, leading to a smaller IR drop of 0.14 V (Fig. 7c) at 3.0 A g⁻¹, and the quasi-rectangular CV profiles at high scan rate of 200 mV s⁻¹ (Fig. S5). The predominated micropore of RP20 as indicated by a large fraction of V_{mic} (Table 1) greatly impedes the ion transport due to its long and tortuous channels, giving rise to a large internal resistance and poor capacitive performance.

The fast ion kinetics enables the KPAC-800 electrode to deliver a high-power capability. Fig. 8 shows the Ragone plots of KPAC-800 electrode in both KOH and TEABF₄/AN electrolyte. The KPAC-800-based capacitor is capable of delivering a specific energy of 8.2 Wh kg⁻¹ at a power density of 100 W kg⁻¹ in aqueous electrolyte. Even at very high power density of 13 kW kg⁻¹, a specific energy of 4.7 Wh kg⁻¹ can still be achieved. Such high power capability matches well with its remarkable rate performance (Fig. 6b) and excellent capacitance retention (Fig. 6d). The wide voltage window of 0–2.5 V in TEABF₄/AN electrolyte enables a higher specific energy of 31.7 and 18 Wh kg⁻¹ to be delivered at power density of 0.62 and 10.6 kW kg⁻¹, respectively, which are far superior to that of RP20-based capacitor.

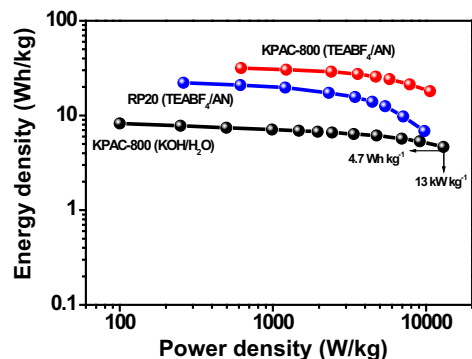


Fig. 8 – Ragone plots of KPAC-800 and RP20-based capacitor in both aqueous and non-aqueous electrolyte. (A color version of this figure can be viewed online.)

4. Conclusions

A facile yet efficient two-step approach has been developed to prepare a highly capacitive porous carbon with shiitake mushroom as the carbon precursor. The first step involved the preliminary activation of shiitake mushroom with H₃PO₄ at 500 °C, while the second step was to further activate the carbon product with KOH at 800 °C. The nanopores formed by H₃PO₄ activation provided sufficient space for accommodating KOH, leading to an effective activation in the second step. With the hierarchically porous framework combining micro-, meso- with macropores, the KPAC-800 electrode exhibited a superior capacitive performance as compared with commercial RP20, including high specific capacitance,

good rate capability and extraordinary cycling stability in both aqueous and non-aqueous electrolyte. These excellent capacitive performances make KPAC-800 one of the promising candidates for electrochemical energy storage. The synthetic route reported herein also holds great potential for large-scale production of functional carbon materials using various nature biomasses as starting materials.

Acknowledgements

This work was financially supported by the National Nature Science Foundations of China (Grant No. 21373134), Fundamental Research Funds for the Central Universities (Grant No: GK201403005, GK201301002, GK201501007), the foundation of returned overseas scholar, MOE, and the Program for Key Science & Technology Innovation Team (2012KCT-21) and Nature Science Foundation of Shaanxi Province (2013JM2001).

Appendix A. Supplementary data

Supplementary data associated with this article can be found, in the online version, at <http://dx.doi.org/10.1016/j.carbon.2015.05.056>.

REFERENCES

- [1] Simon P, Gogotsi Y. Capacitive energy storage in nanostructured carbon–electrolyte systems. *Acc Chem Res* 2013;46:1094–103.
- [2] Yan J, Wang Q, Wei T, Fan Z. Recent advances in design and fabrication of electrochemical supercapacitors with high energy densities. *Adv Energy Mater* 2014;4:1300816.
- [3] Beidaghi M, Gogotsi Y. Capacitive energy storage in micro-scale devices: recent advances in design and fabrication of micro-supercapacitors. *Energy Environ Sci* 2014;7:867–84.
- [4] Simon P, Gogotsi Y. Materials for electrochemical capacitors. *Nat Mater* 2008;7:845–54.
- [5] Lei Z, Lu L, Zhao XS. The electrocapacitive properties of graphene oxide reduced by urea. *Energy Environ Sci* 2012;5:6391–9.
- [6] Jiang H, Lee PS, Li C. 3D carbon based nanostructures for advanced supercapacitors. *Energy Environ Sci* 2013;6:41–53.
- [7] Zhang LL, Zhao XS. Carbon-based materials as supercapacitor electrodes. *Chem Soc Rev* 2009;38:2520–31.
- [8] Pech D, Brunet M, Durou H, Huang P, Mochalin V, Gogotsi Y, et al. Ultrahigh-power micrometre-sized supercapacitors based on onion-like carbon. *Nat Nanotechnol* 2010;5:651–4.
- [9] Lei Z, Liu Z, Wang H, Sun X, Lu L, Zhao XS. A high-energy-density supercapacitor with graphene-CMK-5 as the electrode and ionic liquid as the electrolyte. *J Mater Chem A* 2013;1:2313–21.
- [10] Sevilla M, Mokaya R. Energy storage applications of activated carbons: supercapacitors and hydrogen storage. *Energy Environ Sci* 2014;7:1250–80.
- [11] Hulicova-Jurcakova D, Seredych M, Lu GQ, Bandosz TJ. Combined effect of nitrogen- and oxygen-containing functional groups of microporous activated carbon on its electrochemical performance in supercapacitors. *Adv Funct Mater* 2009;19:438–47.
- [12] Liu R-L, Liu Y, Zhou X-Y, Zhang Z-Q, Zhang J, Dang F-Q. Biomass-derived highly porous functional carbon fabricated by using a free-standing template for efficient removal of methylene blue. *Bioresour Technol* 2014;154:138–47.
- [13] Wang L, Zhang Q, Chen S, Xu F, Chen S, Jia J, et al. Electrochemical sensing and biosensing platform based on biomass-derived macroporous carbon materials. *Anal Chem* 2014;86:1414–21.
- [14] Chen P, Wang L-K, Wang G, Gao M-R, Ge J, Yuan W-J, et al. Nitrogen-doped nanoporous carbon nanosheets derived from plant biomass: an efficient catalyst for oxygen reduction reaction. *Energy Environ Sci* 2014;7:4095–103.
- [15] Qian W, Sun F, Xu Y, Qiu L, Liu C, Wang S, et al. Human hair-derived carbon flakes for electrochemical supercapacitors. *Energy Environ Sci* 2014;7:379–86.
- [16] Gao S, Chen Y, Fan H, Wei X, Hu C, Luo H, et al. Large scale production of biomass-derived N-doped porous carbon spheres for oxygen reduction and supercapacitors. *J Mater Chem A* 2014;2:3317–24.
- [17] K-l Hong, Qie L, Zeng R, Z-q Yi, Zhang W, Wang D, et al. Biomass derived hard carbon used as a high performance anode material for sodium ion batteries. *J Mater Chem A* 2014;2:12733–8.
- [18] Ren Y, Zhang J, Xu Q, Chen Z, Yang D, Wang B, et al. Biomass-derived three-dimensional porous N-doped carbonaceous aerogel for efficient supercapacitor electrodes. *RSC Adv* 2014;4:23412–9.
- [19] Ruan C, Ai K, Lu L. Biomass-derived carbon materials for high-performance supercapacitor electrodes. *RSC Adv* 2014;4:30887–95.
- [20] Wang L, Zheng Y, Zhang Q, Zuo L, Chen S, Chen S, et al. Template-free synthesis of hierarchical porous carbon derived from low-cost biomass for high-performance supercapacitors. *RSC Adv* 2014;4:51072–9.
- [21] Wang H, Li Z, Mitlin D. Tailoring biomass-derived carbon nanoarchitectures for high-performance supercapacitors. *ChemElectroChem* 2014;1:332–7.
- [22] Wu X-L, Wen T, Guo H-L, Yang S, Wang X, Xu A-W. Biomass-derived sponge-like carbonaceous hydrogels and aerogels for supercapacitors. *ACS Nano* 2013;7:3589–97.
- [23] Jiang J, Zhu J, Ai W, Fan Z, Shen X, Zou C, et al. Evolution of disposable bamboo chopsticks into uniform carbon fibers: a smart strategy to fabricate sustainable anodes for Li-ion batteries. *Energy Environ Sci* 2014;7:2670–9.
- [24] Yao H, Zheng G, Li W, McDowell MT, Seh Z, Liu N, et al. Crab shells as sustainable templates from nature for nanostructured battery electrodes. *Nano Lett* 2013;13:3385–90.
- [25] Liu H-J, Wang X-M, Cui W-J, Dou Y-Q, Zhao D-Y, Xia Y-Y. Highly ordered mesoporous carbon nanofiber arrays from a crab shell biological template and its application in supercapacitors and fuel cells. *J Mater Chem* 2010;20:4223–30.
- [26] Lotfabad EM, Ding J, Cui K, Kohandehghan A, Kalisvaart WP, Hazelton M, et al. High-density sodium and lithium ion battery anodes from banana peels. *ACS Nano* 2014;8:7115–29.
- [27] Wang R, Wang P, Yan X, Lang J, Peng C, Xue Q. Promising porous carbon derived from celctue leaves with outstanding supercapacitance and CO₂ capture performance. *ACS Appl Mater Interfaces* 2012;4:5800–6.
- [28] Jiang L, Yan J, Hao L, Xue R, Sun G, Yi B. High rate performance activated carbons prepared from ginkgo shells for electrochemical supercapacitors. *Carbon* 2013;56:146–54.
- [29] Zhang L, Yang X, Zhang F, Long G, Zhang T, Leng K, et al. Controlling the effective surface area and pore size distribution of sp² carbon materials and their impact on the capacitance performance of these materials. *J Am Chem Soc* 2013;135:5921–9.
- [30] Dutta S, Bhaumik A, Wu KCW. Hierarchically porous carbon derived from polymers and biomass: effect of interconnected

- pores on energy applications. *Energy Environ Sci* 2014;7:3574–92.
- [31] Zhang L, Zhang F, Yang X, Long GK, Wu YP, Zhang TF, et al. Porous 3D graphene-based bulk materials with exceptional high surface area and excellent conductivity for supercapacitors. *Sci Rep* 2013;3:1408.
- [32] Wu Z-S, Sun Y, Tan Y-Z, Yang S, Feng X, Müllen K. Three-dimensional graphene-based macro- and mesoporous frameworks for high-performance electrochemical capacitive energy storage. *J Am Chem Soc* 2012;134:19532–5.
- [33] Wang DW, Li F, Liu M, Lu GQ, Cheng HM. 3D aperiodic hierarchical porous graphitic carbon material for high-rate electrochemical capacitive energy storage. *Angew Chem Int Ed* 2008;47:373–6.
- [34] Sun X, Cheng P, Wang H, Xu H, Dang L, Liu Z, et al. Activation of graphene aerogel with phosphoric acid for enhanced electrocapacitive performance. *Carbon* 2015;92:1–10.
- [35] Myglovets M, Poddubnaya OI, Sevastyanova O, Lindstrom ME, Gawdzik B, Sobiesiak M, et al. Preparation of carbon adsorbents from lignosulfonate by phosphoric acid activation for the adsorption of metal ions. *Carbon* 2014;80:771–83.
- [36] Zhang J, Zhao XS. On the configuration of supercapacitors for maximizing electrochemical performance. *ChemSusChem* 2012;5:818–41.
- [37] Zheng X, Lv W, Tao Y, Shao J, Zhang C, Liu D, et al. Oriented and interlinked porous carbon nanosheets with an extraordinary capacitive performance. *Chem Mater* 2014;26:6896–903.
- [38] Wang SW, Tristan F, Minami D, Fujimori T, Cruz-Silva R, Terrones M, et al. Activation routes for high surface area graphene monoliths from graphene oxide colloids. *Carbon* 2014;76:220–31.
- [39] Zhu YW, Murali S, Stoller MD, Ganesh KJ, Cai WW, Ferreira PJ, et al. Carbon-based supercapacitors produced by activation of graphene. *Science* 2011;332:1537–41.
- [40] Wang JC, Kaskel S. KOH activation of carbon-based materials for energy storage. *J Mater Chem* 2012;22:23710–25.
- [41] Jin Z, Yan X, Yu Y, Zhao G. Sustainable activated carbon fibers from liquefied wood with controllable porosity for high-performance supercapacitors. *J Mater Chem A* 2014;2:11706–15.
- [42] Puziy AM, Poddubnaya OI, Socha RP, Gurgul J, Wisniewski M. XPS and NMR studies of phosphoric acid activated carbons. *Carbon* 2008;46:2113–23.
- [43] Fu R, Liu L, Huang W, Sun P. Studies on the structure of activated carbon fibers activated by phosphoric acid. *J Appl Polym Sci* 2003;87:2253–61.
- [44] Deng L, Young RJ, Kinloch IA, Abdelkader AM, Holmes SM, De Haro-Del Rio DA, et al. Supercapacitance from cellulose and carbon nanotube nanocomposite fibers. *ACS Appl Mater Interfaces* 2013;5:9983–90.
- [45] Chen L-F, Huang Z-H, Liang H-W, Gao H-L, Yu S-H. Three-dimensional heteroatom-doped carbon nanofiber networks derived from bacterial cellulose for supercapacitors. *Adv Funct Mater* 2014;24:5104–11.
- [46] Lei ZB, Christov N, Zhang LL, Zhao XS. Mesoporous carbon nanospheres with an excellent electrocapacitive performance. *J Mater Chem* 2011;21:2274–81.
- [47] Stoller MD, Ruoff RS. Best practice methods for determining an electrode material's performance for ultracapacitors. *Energy Environ Sci* 2010;3:1294–301.
- [48] Taberna PL, Simon P, Fauvarque JF. Electrochemical characteristics and impedance spectroscopy studies of carbon-carbon supercapacitors. *J Electrochem Soc* 2003;150:A292–300.
- [49] Portet C, Yushin G, Gogotsi Y. Effect of carbon particle size on electrochemical performance of EDLC. *J Electrochem Soc* 2008;155:A531–6.
- [50] Wang H, Sun X, Liu Z, Lei Z. Creation of nanopores on graphene planes with MgO template for preparing high-performance supercapacitor electrodes. *Nanoscale* 2014;6:6577–84.
- [51] Xu Y, Lin Z, Zhong X, Huang X, Weiss NO, Huang Y, et al. Holey graphene frameworks for highly efficient capacitive energy storage. *Nat Commun* 2014;5:4554–61.
- [52] Fic K, Lota G, Meller M, Frackowiak E. Novel insight into neutral medium as electrolyte for high-voltage supercapacitors. *Energy Environ Sci* 2012;5:5842–50.
- [53] Chmiola J, Largeot C, Taberna PL, Simon P, Gogotsi Y. Desolvation of ions in subnanometer pores and its effect on capacitance and double-layer theory. *Angew Chem Int Ed* 2008;47:3392–5.
- [54] Zhang LL, Zhao X, Stoller MD, Zhu Y, Ji H, Murali S, et al. Highly conductive and porous activated reduced graphene oxide films for high-power supercapacitors. *Nano Lett* 2012;12:1806–12.